Journal of The
Electrochemical Society

Self-Healing Effect of Hybrid Sol-Gel Coatings Based on GPTMS, TEOS, SiO_2 Nanoparticles and $Ce(NO_3)_3$ Applied on Aluminum Alloy 7075-T6

Self-Healing Effect of Hybrid Sol-Gel Coatings Based on GPTMS, TEOS, SiO_2 Nanoparticles and $Ce(NO_3)_3$ Applied on Aluminum Alloy 7075-T6

Urša Tiringer,[1,2] Alicia Durán,[3] Yolanda Castro,[3] and Ingrid Milošev [1,*,z]

[1] *Department of Physical and Organic Chemistry, Jožef Stefan Institute, SI-1000 Ljubljana, Slovenia*
[2] *Jožef Stefan Postgraduate School, SI-1000 Ljubljana, Slovenia*
[3] *Instituto de Cerámica y Vidrio (CSIC), Campus de Cantoblanco, 28049 Madrid, Spain*

Aluminum alloy AA7075-T6 is most commonly used in the aircraft and automotive industries. Due to the presence of intermetallic particles, AA7075-T6 is susceptible to localized corrosion in chloride solutions. In the present work multilayer hybrid sol-gel coatings, based on silane precursors 3-glycidyloxypropyl(trimethoxysilane) (GPTMS) and tetraethoxysilane (TEOS), were used to protect AA7075-T6 from corrosion. To enrich the barrier properties of the coating, SiO_2 nanoparticles were added to the GPTMS/TEOS sol-gel solution. Inhibition and a self-healing effect were achieved by doping $Ce(NO_3)_3$ in the coating. A multi-layer system was applied on the substrate composed of a first layer doped with $Ce(NO_3)_3$ and the second, undoped sol-gel layer. The addition of cerium increases the lifespan of hybrid sol-gel coating and has a role in self-healing if it is locked within the first layer of the multilayer coating. The self-healing effect was confirmed by immersion of unscribed and scribed coated substrates in 0.1 mol/L NaCl by using the immersion test, electrochemical impedance spectroscopy, X-ray photoelectron spectroscopy and scanning electron microscopy with chemical analysis.

 [DOI: 10.1149/2.0211805jes]

Manuscript submitted December 5, 2017; revised manuscript received March 6, 2018. Published March 17, 2018.

Due to increasing demand for light-weight metals to reduce fuel consumption and, consequently, CO_2 emission, aluminum alloy AA7075-T6 is very attractive in automotive and aircraft industries. In addition to its low density, its advantages are high strength-to-weight ratio and good mechanical properties.[1–3] However, due to the presence of zinc and copper intermetallic particles, AA7075-T6 readily undergoes localized corrosion, which limits its use in more aggressive environments. Chromate conversion coatings (CCCs), which were used for decades as providing the most effective corrosion protection of aluminum alloys, are limited, in the European Union.[4] Many surface treatments have been proposed to replace CCCs, the sol-gel process being one of the most promising and environmentally friendly.[5–12] In hybrid sol-gel coatings, which combine inorganic and organic compounds, the inorganic compound provides mechanical support, while the organic compound adds to flexibility and decreases treatment temperature.[8,12–15] Hybrid sol-gel coatings achieve protection of underlying substrate by acting as barrier coatings. Addition of silica nanoparticles (SiO_2) into sol-gel coating has been reported to additionally increase the barrier effect by increasing the coating thickness, density and reinforcement.[16–23] Still, if these coatings do not contain corrosion inhibitors they lack the ability to inhibit the corrosion process once it commences, i.e. they do not show active inhibition ability resulting in a self-healing of the coating.

To obtain an active corrosion protection, corrosion inhibitors can be incorporated into sol-gel coating. According to Hinton et al.,[24,25] many salts of rare earth ions such as Ce^{3+}, Y^{3+}, La^{3+}, Pr^{3+} and Nd^{3+}, are successful corrosion inhibitors for aluminum alloys, Ce^{3+} being the most efficient. When added directly to corrosive solution, e.g. chloride solution, earth salts hydrolyse and can then precipitate at the metal surface once the conditions for precipitation are established; in the case of Ce, cerium (III) hydroxide $Ce(OH)_3$ precipitates at the cathodic sites at the surface where the pH increases due to formation of OH^- ions during the reduction of oxygen.[26,27] $Ce(OH)_3$ formed can be further oxidized to $Ce(OH)_4$ and insoluble CeO_2, which acts as a protective barrier to oxygen and lowers the cathodic activity by hindering the transfer of electrons from the anodic to cathodic sites.[28–30] The addition of corrosion inhibitors, including cerium, to the formulation based on precursors, such as tetramethylorthosilicate (TMOS), tetraethoxysilane (TEOS), methyltrimethoxysilane (MTMS), 3-glycidoxypropyltrimethoxysilane (GPTMS), etc.[8] has been shown to provide self-healing properties when these coatings are applied on aluminum alloys.[21,29,31–35] Thus, when the coating is mechanically damaged or local defects are present, the inhibitor is released and act in such a way to repair the damage or retard the corrosion process. The most probable self-healing mechanism involves the formation of $Ce(OH)_2^{2+}$ ions which can migrate to the damaged sites where are converted into highly insoluble $Ce(OH)_4/CeO_2$.[28,36–38] Another possibility to express self-healing ability in silane hybrid sol-gel coating was pre-treatment of aluminum alloy in a $1 \cdot 10^{-3}$ mol/L $Ce(NO_3)_3$ solution.[37]

The possible drawback of direct incorporation of cerium ions into the hybrid coating is the generation of high porosity and consequently fast release of inhibitor into the solution which prevents the long-term self-healing ability.[39–41] Further, the increased roughness of cerium containing coatings was noticed and ascribed to a superficial agglomeration/precipitation of cerium containing nanoparticles.[32] This implicates that there exist an optimal content of Ce which would not deteriorate the coating stability but yet provide a self-healing ability for a reasonably long period of time upon exposure to chloride solution. This task is difficult to achieve, as shown in our previous study.[40,41] When using monolayer sol-gel coating doped with cerium to obtain barrier and active protection, the long-term coating stability can be jeopardized.[16,40–42] Namely, the inhibition effect was observed, but a fast deterioration of the barrier properties of the coating occurred after 24 hours in 0.35 wt% NaCl.[16] A multi-layer sol-gel hybrid coating, based on TEOS, methacryloxypropyl trimethoxysilane (MPS), ethylene glycol dimethacrylate (EGDMA) and glycidyl methacrylate (GMA) containing an intermediate cerium doped layer was shown to greatly improve the corrosion properties of AA2024.[32] It was further showed that the barrier and active protection of coatings were improved in multi-layer coating, based on TEOS, GPTMS and SiO_2 nanoparticles, where cerium was in the top layer, but the self-healing ability of such coatings applied on carbon steel was not confirmed.[16]

In the present work three types of multi-layer hybrid sol-gel coatings were developed based on the inorganic precursor TEOS, organic precursor GPTMS, SiO_2 nanoparticles and corrosion inhibitor $Ce(NO_3)_3$. The aim was to develop a coating system that would prevent the leaching of cerium ions from the coating. Thus, a multilayer

*Electrochemical Society Member.
[z]E-mail: ingrid.milosev@ijs.si

system of two different coatings was used: the first layer was doped with cerium, while the second was undoped to increase the stability of cerium in the underlying layer. This multi-layer system was expected to enable self-healing through migration of cerium ions to damaged sites and the recovery of damaged sites (i.e. self-healing) in the course of prolonged immersion in chloride containing electrolyte. We planned the experiments in such a manner as to prove the self-healing effect particularly on scribed coatings. A further novelty of the present work is the type of aluminum alloy used, i.e. AA7075-T6 which is difficult to protect due to its high susceptibility for localized corrosion in chloride environment.

Experimental

Metal substrate preparation.—Aluminum alloy AA7075-T6 (Zn 5.81 wt%, Mg 2.55 wt%, Cu 1.67 wt%, Fe 0.21 wt%, Si 0.08 wt%, the remaining Al) with dimensions of 30 mm × 65 mm × 2 mm, supplied by Kaiser Aluminum, was subjected to a three-step cleaning procedure including alkaline cleaning (Metaclean T2001 – Chemie Vertrieb Hannover GmbH & Co KG), an alkaline etching (Turco Liquid Aluminetch Nr.2 – Turco Chemie GmbH) and a final step of acid desmutting (Turco Liquid Smutgo NC – Turco Chemie GmbH). After each step samples were rinsed with deionized water.

Synthesis of hybrid sols and coatings deposition.—The schematic presentation of sol synthesis and coating deposition and curing are presented in Figs. 1 and 2a. Two hybrid sols were prepared, one undoped and the other doped with cerium (Fig. 1). The first sol was prepared at room temperature by mixing tetraethoxysilane (TEOS, Aldrich, 99%) and 3-(glycidyloxypropyl)trimethoxy silane (GPTMS, ABCR, 98%) with a colloidal silica (SiO_2) suspension (Ludox-4S, Aldrich, aqueous suspension 40 wt%, particle size 20 nm, pH 9). After 30 minutes of stirring, 0.6 mL of concentrated nitric acid HNO_3 (VWR, 65%) was added to 100 mL of solution as a catalyst. Finally, absolute ethanol (EtOH, Panreac, 99.8%) was added as a dissolvent. The final silica concentration was 120 g/L, with 64 g/L of colloidal particles, labelled as 120 (64). The molar ratio of the first hybrid sol was TEOS/GPTMS/SiO_2 = 0.4/0.46/0.14 and it was denoted as GTS.

The second sol was prepared following the same process, but incorporating cerium as a corrosion inhibitor. Cerium nitrate ($Ce(NO_3)_3$ .6 H_2O, Aldrich, 98%), dissolved in EtOH, was added before addition of the catalyst (HNO_3). The molar ratio of the second sol was TEOS/GPTMS/SiO_2/Ce = 0.39/0.44/0.12/0.05, denoted as GTS-Ce.

After synthesis, sols were immediately deposited on AA7075-T6 substrate by dip-coating at a withdrawal rate of 30 cm/min. Three different coatings were prepared (Fig. 2a). The first coating was prepared by the deposition of two layers of GTS sols (denoted as GTS), and the second by the deposition of two layers of GTS-Ce sols (denoted as GTS-Ce). Before depositing the second layer the first layer was dried using a hot air gun at 100°C for 3 minutes. The third coating was the combination of GTS-Ce and GTS sols (denoted as GTS-Ce+GTS). Each sol was deposited as a single layer, with intermediate curing using a hot air gun at 100°C for 3 minutes.

Finally, the coatings were cured as follows: using a ramp of 5°C/min from room temperature up to the curing temperature of 120°C, cured for 1 h, and then cooled down with the same rate 5°C/min to reach room temperature (Fig. 2a).

Coating characterization.—The coating thickness was measured on coated glass-slides by Spectroscopic Ellipsometer (J.A. Woollam Co., Inc, EC-400, M-2000 U Software: WVASE32). The spectral band was recorded from 250 nm to 900 nm at incident angles between 50° and 60°. The data were fitted using the WVASE32 software with a Cauchy model. Three measurements were performed for each sample at different sites and the mean value was deduced for each coating.

The morphology and composition of coatings were analyzed using a field emission scanning electron microscope (FE-SEM, JEOL JSM-7600F) equipped with energy dispersive X-ray spectrometer (EDS, Oxford Instruments INCA). The diameter of the analyzed area was a few micrometres and the analyzed depth around 1 μm. Prior to analysis, samples were coated with a carbon layer to reduce the charging effect. Images were recorded in a compositional mode using an energy of 15 kV. EDS mapping was performed with a resolution of 512 lines.

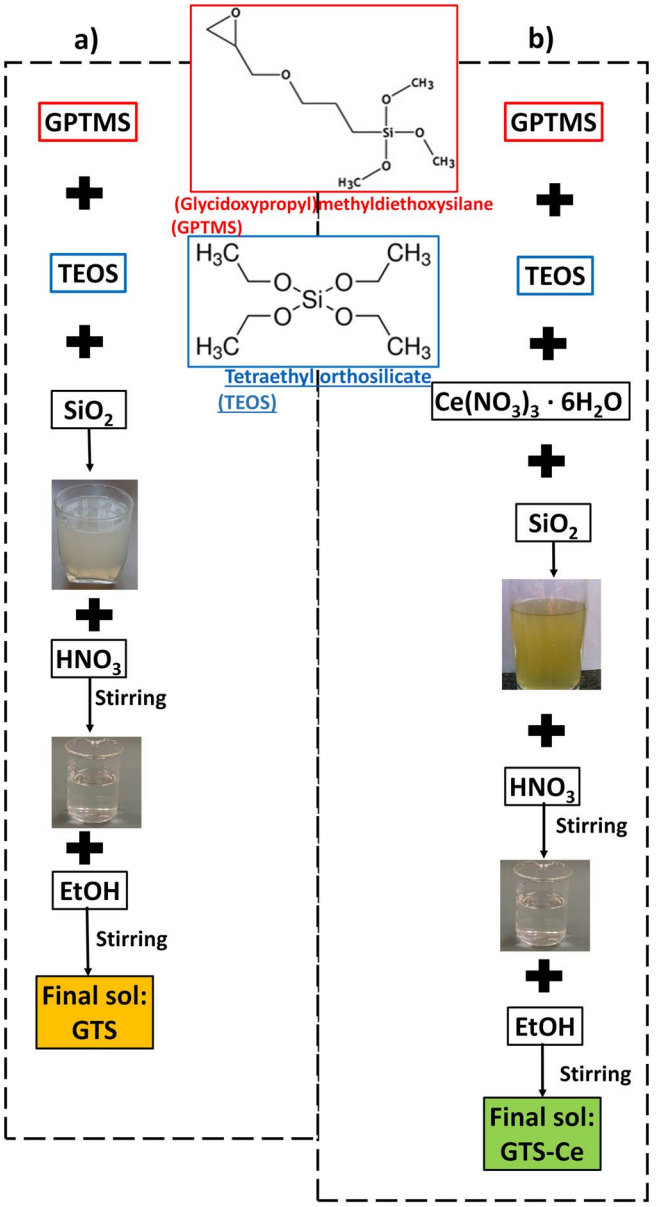

Figure 1. Schematic presentation of synthesis of hybrid sols GTS and GTS-Ce.

Ultraviolet-visible (UV-vis) spectra (Perkin with Elmer Lambda 950 spectrophotometer) were acquired between 200 and 700 nm for coatings deposited on SiO_2 substrates. Spectrum for the uncoated SiO_2 substrate was recorded for reference.

X-ray photoelectron spectroscopy (XPS) was carried out using a PHI-TFA XPS spectrometer (Physical Electronic Inc.). The vacuum during the XPS analysis was in the range of 10^{-9} mbar. The analyzed area was 0.4 mm in diameter and the depth about 3–5 nm. X-rays were provided from a monochromatic Al source at photon energy of 1486.6 eV. XPS spectra were analyzed by Multipak software, version 8.0 (Physical Electronics Inc.). The elemental composition was determined from survey spectra. An Ar^+ ion beam, with an energy of 4 keV and a raster of 3 mm × 3 mm, was used for etching. The sputtering rate was 2 nm/min, as determined on a Ni/Cr multilayer structure of known thickness.

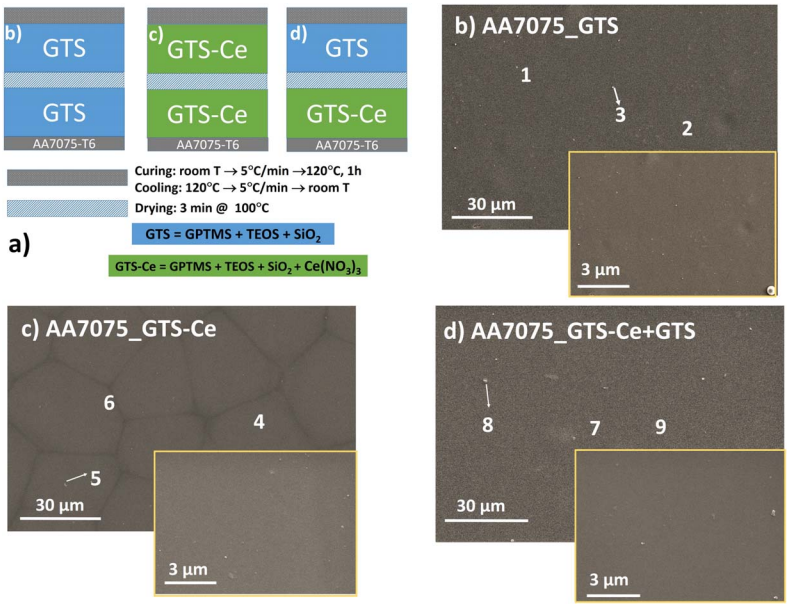

Figure 2. (a) Schematic presentation of the coatings GTS, GTS-Ce and GTS-Ce+GTS and drying and curing treatments. SEM images of AA7075-T6 coated with (b) GTS, (c) GTS-Ce and (d) GTS-Ce+GTS coatings. The numbers 1–9 denote locations where EDS analysis was carried out (Table I). Note that all coatings are bilayer coatings.

Corrosion behavior of coatings.—The corrosion performance of uncoated and coated AA7075-T6 substrates was tested using electrochemical impedance spectroscopy (EIS) in a 0.1 mol/L NaCl aqueous solution at room temperature. An AUTOLAB PGSTAT 12 potentiostat/galvanostat, controlled by NOVA 1.11 software, was used for measurements made in a three-electrode standard corrosion cell (PAR Flat cell K0235, volume 250 mL). An Ag/AgCl/saturated KCl electrode was the reference electrode (0.192 V versus standard hydrogen electrode), the platinum mesh was a counter electrode and the tested material embedded in a Teflon holder was a working electrode. The area exposed to the corrosion medium was 1 cm^2. All potentials in the text are given with respect to an Ag/AgCl electrode. The EIS were performed at open circuit potential with an ac excitation voltage of 10 mV in the range from 10^{-2} Hz to 10^5 Hz. Corrosion resistance was assessed by determining the modulus of impedance, Z, from the Bode plot (Z vs. frequency) at a frequency of 10^{-2} Hz. Experiments were repeated at least three times and the most highly representative measurement was chosen for plotting.

The development of corrosion process on uncoated and coated substrates were also monitored by an immersion test carried out in 0.1 mol/L NaCl at room temperature. Samples were placed in a DURAN glass flask containing 300 mL NaCl solution. The area of sample exposed to electrolyte was 1450 mm^2, giving a ratio of 0.207, thus in accordance with the "Standard guide for laboratory immersion corrosion testing of metals" (NACE TMO 169/631). Immersed samples were monitored for 80 days.

Evaluation of the self-healing effect on scribed coatings.—To evaluate the self-healing property of coatings, the samples were scribed and the course of self-healing process was followed using different methods. Two types of scribe were created: (i) a cross shaped scribe, with a depth of over 7 µm, made with a diamond tip; the depth of the scribe was larger than the coating depth and reached the underlying substrate, and (ii) cross shaped indents, with a depth around 2–4 µm, made using a Vickers diamond indenter within the coating depth. The indents were made using a Fisherscope H100C tester at the indentation load 2 N. The depth of the scribe was determined by the profilometer (model Bruker DektakXT). The radius of the stylus was 2 µm; it was used at a force of 30 mN. Map resolution was 10 µm/trace, scanned at a spot size of 1 mm × 1 mm. The vertical analysis range was 65.5 µm and the vertical resolution 0.167 µm/point. Data was processed using Bruker Vision 64 and TalyMap Gold 6.2 software. Three measurements were performed at different sites of the scribe and the mean value was determined.

Scribed GTS, GTS-Ce and GTS-Ce+GTS coatings were exposed to the 0.1 mol/L NaCl solution for various immersion times to follow the self-healing. EIS spectra were recorded during the course of immersion. The morphological changes at the scribe were monitored as a function of immersion time using an optical microscope (Olympus BX51). The magnification and light were controlled and kept constant throughout the experiment. At the end of the immersion test, SEM/EDS and XPS analyses were carried out.

Results and Discussion

The morphology, composition and corrosion properties of the uncoated and coated AA7075-T6 samples were analyzed. The study was divided into three parts: (i) characterization of as-prepared coatings, (ii) corrosion behavior of unscribed coatings and (iii) corrosion behavior of scribed coatings.

Coating characterization.—*Ellipsometry.*—The thickness of GTS, GTS-Ce and GTS-Ce+GTS coatings deposited on glass-slides was measured by ellipsometry. The total thickness of GTS coating was 5.3 ± 0.4 µm, of GTS-Ce was 7.0 ± 0.7 µm and of GTS-Ce + GTS coating was 6.0 ± 0.6 µm. The GTS-Ce coating was thicker as a result of the presence of cerium, which was ascribed to increased porosity, i.e. free volumes in the hybrid network, as will be described below.[44–46]

SEM/EDS analysis.—The morphology and composition of different coatings applied on AA7075-T6 were investigated by SEM/EDS analysis (Fig. 2, Table I). The surface of the GTS coating applied on AA7075-T6 was shown by SEM/EDS analysis to be homogeneous (Fig. 2b). EDS analysis shows Si and O as only elements of the coatings; Al and alloying elements were not detected, since the coating thickness was greater than 5 µm.[43] The concentrations of Si and O at locations 1, 2 and 3 were similar, indicating homogeneous composition over the surface. At the surface of GTS-Ce coating in addition to Si and O, a small concentration of Ce (up to 1 at.%) was identified at all three locations 4, 5 and 6 (Fig. 2c, Table I). Although the coating was homogeneous as GTS, some underlying structure in the form of grains is evident (Fig. 2c). This may be caused by the incorporation of cerium. It has been shown that the addition of cerium affects the structure of the hybrid sols in several ways: Ce promotes inorganic and organic polymerization of the network and the process of opening of the epoxy ring.[46] The degree of this effect is, however, dependent on Ce concentration in the sol. When Ce is present at low concen-

Table I. Concentrations of elements obtained by EDS analysis at various locations on the AA7075-T6 alloy coated with GTS (locations 1–3), GTS-Ce (locations 4–6) and GTS-Ce+GTS (locations 7–9) coatings. Locations are denoted on SEM images in Fig. 2.

Location	Si [at.%]	O [at.%]	Ce [at.%]
1	37.7	62.3	/
2	34.7	65.3	/
3	33.3	66.7	/
4	35.3	63.8	0.9
5	35.3	64.0	0.7
6	36.9	62.5	0.6
7	35.1	64.9	/
8	37.4	62.6	/
9	33.8	66.2	/

tration, the condensation and polymerization of both inorganic and organic networks are favored. When present at higher concentrations (> 0.01 mol/L), the polymerization of inorganic network is favored and may lead to destabilization of the Si−O−Si structure and possible creation of free volumes (pores) in the hybrid.[46] Atomic radius of Ce is larger than that of Si (185 and 110 pm, respectively) which is another factor which can cause internal stress. The Ce concentration used herein is 0.05 mol/L, which may already be in the range when destabilization of the network may occur leading to the structure observed in Fig. 2c. However, this higher Ce concentration may be beneficial for the self-healing effect, as will be shown below. The surface of the GTS-Ce+GTS coating was homogeneous and similar to that of GTS, as confirmed by EDS analysis (Fig. 2d). The absence of cerium at the surface of the GTS-Ce+GTS coating confirms that the deposition of the second layer (GTS) completely covered the underlying GTS-Ce layer. No structure similar to that in GTS-Ce (Fig. 2c) was observed indicating that the outer GTS layer does not destabilize the coating structure and that incorporated cerium was locked in the inner layer, closer to metal surface.

EDS analysis confirmed the presence of cerium but it could not differentiate between two oxidation states Ce^{3+} and Ce^{4+}. UV-vis analysis is explored for that purpose. UV-vis spectra recorded on uncoated SiO_2 substrate and substrates coated with GTS-Ce and with GTS-Ce+GTS coatings are presented in Fig. 3. The GTS-Ce coating absorbs some visible light in the range from 300 to 500 nm. Since Ce^{3+} ions are colorless and Ce^{4+} are yellow, this coating contains at least some amount of cerium ions in Ce^{4+} oxidation state. Although Ce is added in the sol in the form of Ce^{3+}, during the sol-gel synthesis

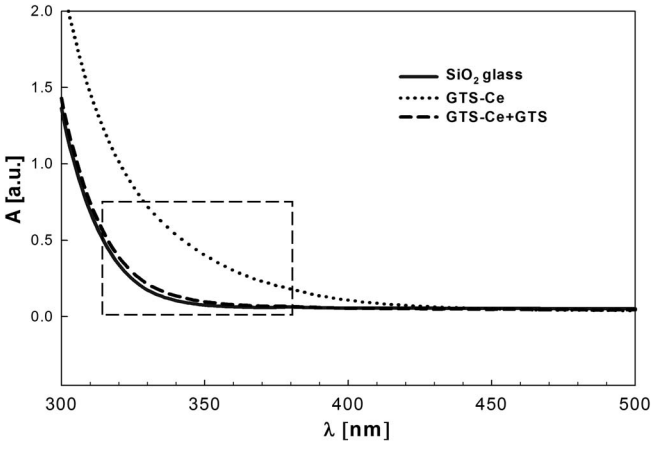

Figure 3. UV-vis-NIR spectra of uncoated SiO_2 and SiO_2 coated with GTS-Ce and GTS-Ce+GTS in the range from 300 to 700 nm. Coatings were cured from a room temperature, with a ramp of 5°C/min, up to the 120°C and cured for 1 hour at 120°C.

and especially during curing process at 120°C it can be partially oxidized to Ce^{4+}, as evident by slightly yellow coloration of the coating. In contrast, UV-vis spectrum for the GTS-Ce+GTS coating shows only a slightly different curve compared to substrate, i.e. no evidence of Ce(IV). After curing at 120°C, the coating remained colorless and not yellow as GTS-Ce coating. Although both coatings (GTS-Ce and GTS-Ce+GTS) contain GTS-Ce as an inner layer (Fig. 2a), the difference between two coatings arises from the curing procedure. Namely, whilst GTS-Ce coating was finally cured for 1 h at 120°C where oxidation of Ce^{3+} to Ce^{4+} can take place, in the case of GTS-Ce+GTS coating the final curing does not affect the underlying GTS-Ce layer and Ce remained mainly as colorless Ce^{3+}. Intermediate drying for 3 min at 100°C was not sufficient to produce significant amount of Ce^{4+} species.

Corrosion behavior of unscribed coatings in nacl solution.—*Electrochemical impedance analysis.*—EIS as a non-destructive method was used to in situ follow the electrochemical properties of the uncoated and coated substrates. The magnitudes of the impedance, $|Z|$, and the phase angle, ϕ, as a function of the frequency, f, (Bode plots) for uncoated and variously coated AA7075-T6 substrates are presented for different immersion time up to 25 days (Fig. 4). The uncoated AA7075-T6 sample shows an EIS spectrum (Figs. 4a, 4b) typical of pitting corrosion, as described by Mansfeld and Wang,[47] i.e. transmission line type impedance and a minimum in the phase angle at lower frequencies. The plot of $|Z|$ vs. f shows transmission at frequencies of 10^1 to 10^0, depending on the immersion time (Fig. 4a). With prolonged immersion the transition shifted to lower frequencies and the impedance increased within one order of magnitude. This may be related to the gradual formation of an oxide layer during the course of immersion which offers a certain degree of protection. In consequence, the maximum of the ϕ vs. f plot shifted to lower frequencies (Fig. 4b) and the phase angle at the lowest frequencies increased.

Coated substrates showed different Bode plots from those of uncoated substrate. The results are interpreted qualitatively in accordance with the modelling of physicochemical processes reported for aluminum alloys coated with hybrid sol-gel coatings incorporating $Ce(NO_3)_3$.[31,48–50] In general, in Bode plots of $|Z|$ vs. f three distinct regions are evident: high frequency range related to the outer part of the coating at the coating/electrolyte interface, intermediate frequency range related to the inner part of the coating and intermediate oxide-based layer formed between Al substrate and sol-gel coating (natural aluminum oxide layer Al−O−Al and Al−O−Si bonds[51] at the substrate/coating interface), and low frequency range related to corrosion process at the inner metal/sol-gel coating interface. During immersion, the pore resistance of the coating as well as the resistance of the intermediate oxide layer are important for compactness of the interface between the substrate and sol-gel coating. Stable and dense interface prevents the formation of conductive pathways and electrolyte ingress to the substrate. This process then leads to the local corrosion process expressed by the double layer capacitance and charge transfer resistance at the low frequency side.

On the immersion, two time constants are present in Bode plots for the GTS coating, at high frequency of 10^5 Hz and intermediate frequency of 1 Hz (Figs. 4c, 4d), related to the sol-gel coating and intermediate oxide layer. Coatings shows some barrier effect evidenced by increased Z in the low frequency range. After 2 days of immersion, a low frequency resistive part appeared, as reflected in the progressive decrease in impedance, probably related to the cracks formed in the intermediate oxide layer that allow ingress of electrolyte. In the ϕ vs. f plot, signs of corrosion at the inner substrate/coating interface (low frequency) were visible at the same time (Fig. 4d). On the high frequency side, reflecting the coating capacitance, the value of ϕ also decreased, indicating deterioration of the coating that progressed further at longer immersion times.

Similar to GTS, the GTS-Ce coating (Figs. 4e, 4f) also shows barrier protection. However, at the low frequency part (inner interface substrate/coating) the resistive part was smaller, and the ϕ vs. f plot showed that the ϕ values were initially much lower, indicating lower

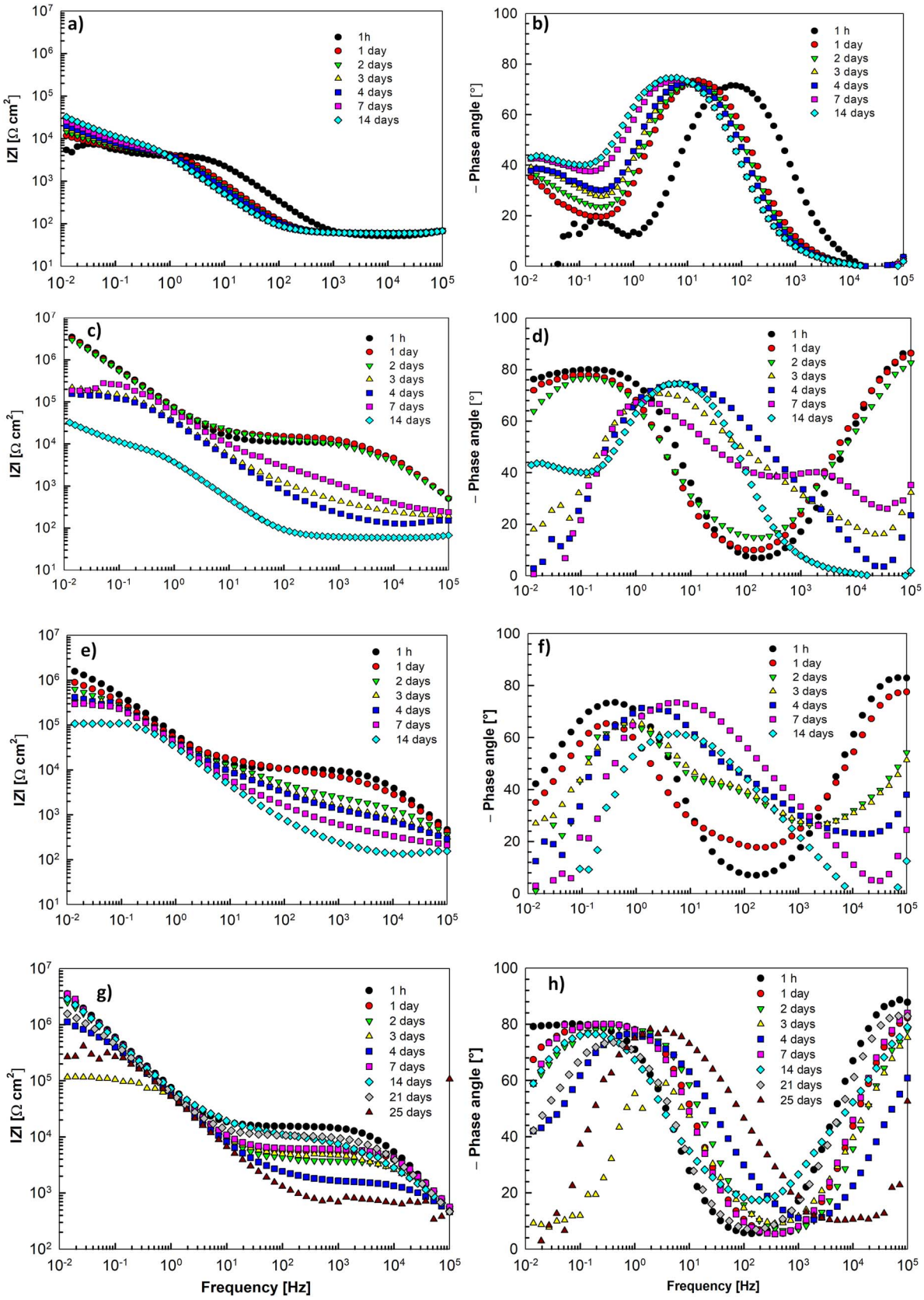

Figure 4. Bode plots of magnitude of impedance and phase angle recorded after various immersion times in 0.1 mol/L NaCl (from 1 h to 25 days) for (a, b) uncoated AA7075-T6, and for AA7075-T6 coated with (c, d) GTS, (e, f) GTS-Ce, and (g, h) GTS-Ce+GTS coatings.

stability of this coating. This may be related to the incorporation of Ce which may destabilize the structure of the coating[46] and/or to progressive release of cerium from the coating which, at the same time, leaves the porous structure underseath susceptible to corrosion.

Finally, the GTS-Ce+GTS coating exhibited behavior that can be attributed to barrier effect and self-healing. Namely, on immersion and up to the following 3 days, trend in the $|Z|$ vs. f plot (Fig. 4g) was similar to that for the GTS coating, i.e. progressive appearance of resistive behavior at low and intermediate frequencies. However, the values of ϕ were high, around -80°, in both high and low frequency regions, indicating stability of the coating (Fig. 4h). After 4 days, the impedance at low frequencies started to increase again, and the values of ϕ at the maximum were high and remained so at low frequencies, which may be ascribed to high charge transfer resistance of Ce-containing multilayer coating.[50] Only after 25 days were signs of corrosion noted — Z at low frequency decreased (Fig. 4g) and ϕ values formed a peak with low values on both low and high frequency sides (Fig. 4h).[48,49]

The impedance value determined at 0.01 Hz in the Bode plot of modulus of impedance vs. frequency was chosen as the parameter representing the corrosion resistance of the coating.[52] Values of $Z_{0.01\ Hz}$ as a function of immersion time are presented for uncoated and coated samples (Fig. 5). The $Z_{0.01\ Hz}$ value of uncoated sample AA7075-T6 gradually increased with time over the first 14 days for approximately one order of magnitude, reaching $2{\cdot}10^4\ \Omega\ cm^2$. The uncoated AA7075-T6 surface is in direct contact with the electrolyte solution and becomes covered by an oxide that gradually forms and acts protectively for a certain period of time.[53] On immersion, the $Z_{0.01\ Hz}$ value of the GTS coated substrate was larger, by more than two orders of magnitude ($Z_{0.01\ Hz} = 4{\cdot}10^6\ \Omega\ cm^2$), than that of the uncoated sample, confirming the barrier protective properties of the coating. After 3 days of immersion the $Z_{0.01\ Hz}$ values decreased gradually, which may be the result of the porous nature of the coating and the diffusion of the chloride anions into the coating where they interact with the substrate. Z values of the GTS-Ce coated sample were, at the beginning of immersion, similar to those of the GTS coating ($1.5{\cdot}10^6\ \Omega\ cm^2$). After 1 day of immersion, however, the value of $Z_{0.01\ Hz}$ decreased, indicating that the almost all cerium was released from the coating. At immersion times longer than 14 days, uncoated and GTS and GTS-Ce coated samples deteriorated but the latter coating still showed higher impedance indicating beneficial effect of Ce addition.

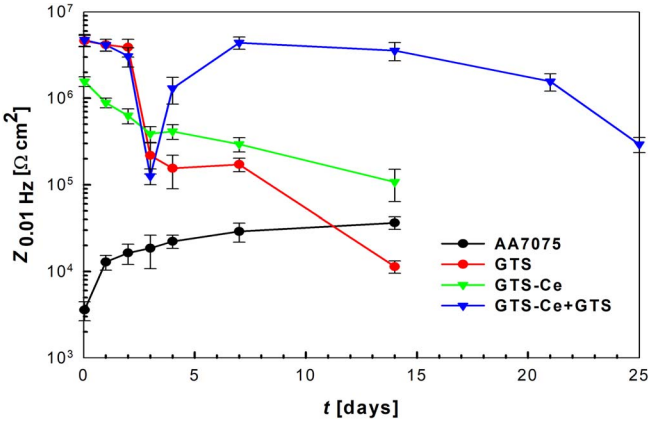

Figure 5. Values of $Z_{0.01\ Hz}$ (impedance at 0.01 Hz determined from Bode plots, Fig. 4) for uncoated and variously coated AA7075-T6 as a function of immersion time in 0.1 mol/L NaCl.

The trend of the $Z_{0.01\ Hz}$ value of the GTS-Ce+GTS coating, however, was different. At the beginning of immersion the value of Z was large, similar to that for the GTS coating ($4{\cdot}10^6\ \Omega\ cm^2$). After 3 days of immersion it was reduced to $10^5\ \Omega\ cm^2$. After 4 days of immersion, however, it again increased, almost to its initial value of $2{\cdot}10^6\ \Omega\ cm^2$ and remained stable for up to 21 days of immersion. After 25 days of immersion, the value of $Z_{0.01\ Hz}$ decreased to $2{\cdot}10^5\ \Omega\ cm^2$ but remained larger compared to other two coatings.

Immersion testing.—The lifespan of differently coated AA7075-T6 samples was followed using the NACE TMO 169/631 immersion test in 0.1 mol/L NaCl for up to 80 days (Fig. 6). Pitting and galvanic corrosion of an uncoated sample was visible after 1 day of immersion. Corrosion of a GTS coating was visible on the borders after

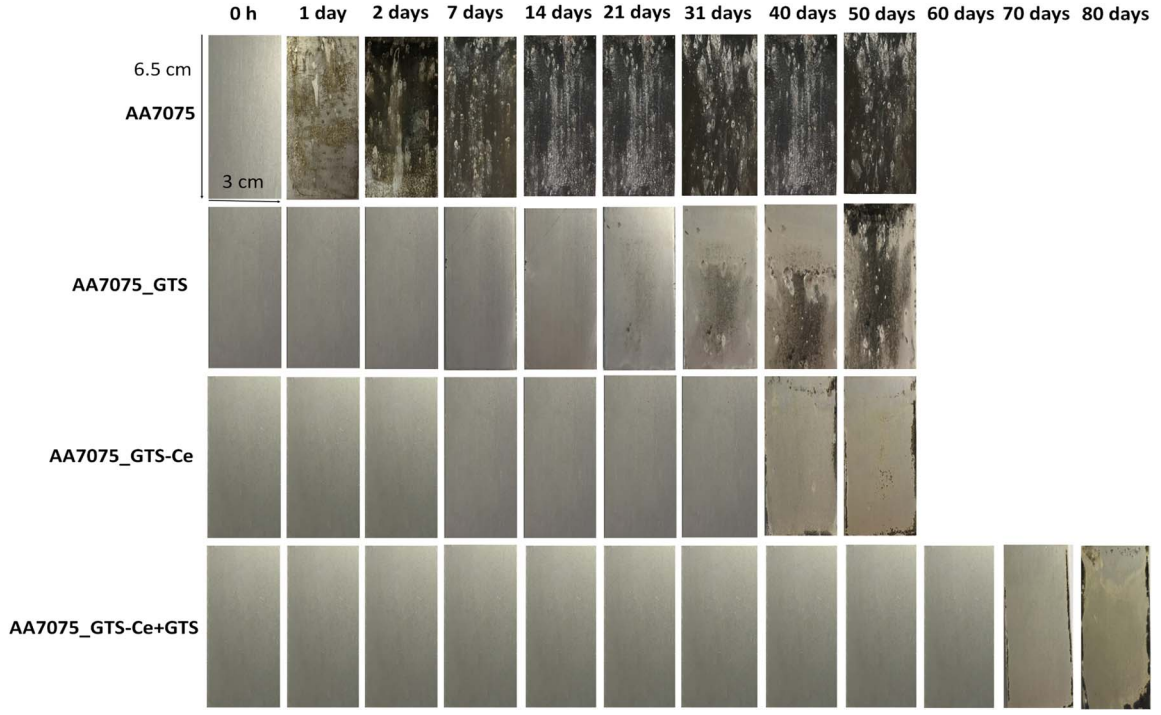

Figure 6. Images of uncoated AA7075-T6 and AA7075-T6 with GTS, GTS-Ce and GTS-Ce+GTS coatings during an immersion test in 0.1 mol/L NaCl at room temperature. Images were taken after different times of immersion up to 80 days (NACE TMO 169/631 immersion test).

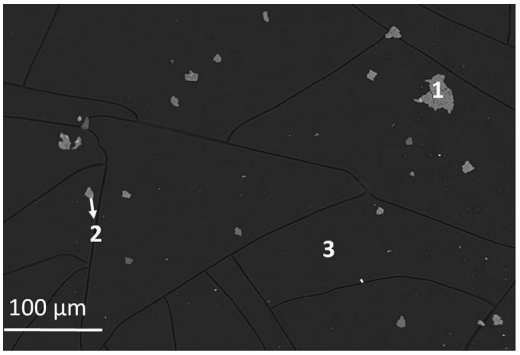

Figure 7. SEM image of AA7075-T6 coated with GTS-Ce+GTS after 4 days of immersion in 0.1 mol/L NaCl. The numbers 1, 2 and 3 on the SEM image denote locations where EDS analysis was carried out (given in Supplement materials as Fig. S1). The SEM image was taken in compositional mode.

7 days and was spread throughout the surface after 21 days. The corrosion resistance of the GTS coating is the result of its good barrier properties.[43] The GTS-Ce coating remained undamaged for 40 days of immersion, which may the result of the active corrosion inhibition caused by cerium. The longest period of resistance to corrosion was observed for samples coated with a GTS-Ce+GTS coating which remained virtually undamaged up to 70 days of immersion, at which point corrosion was observed on the borders. Based on EIS results (Figs. 4, 5) and immersion test (Fig. 6), an efficient protection is observed to GTS-Ce+GTS coating. Thus, even when some pits were formed during 70 days of immersion, they were healed by the action of cerium ions.

SEM/EDS analyses.—To study the role of cerium in the self-healing effect in more detail, AA7075-T6 prepared with a GTS-Ce+GTS coating was immersed for 4 days in 0.1 mol/L NaCl. Samples were then inspected using SEM/EDS (Fig. 7 and Fig. S1). After immersion, numerous bright deposits were shown to be present at the surface. Since images were recorded in compositional mode, the brightness is related to atomic mass. These bright deposits (Fig. 7) contained cerium and oxygen (Fig. S1, spectra at locations 1 and 2), indicating the formation of cerium hydroxide or oxide. In addition to Ce and O, Si was detected as a major element of the surrounding coating. It is known that the deposition of Ce-oxides proceeds at the cathodic sites at the surface which are, in the case of AA7075-T6, Cu-containing intermetallic particles (IMPs).[54–59] The fact that no Cu could be identified at the intermetallic particles proves that the deposits of Ce hydroxide/oxide are thicker than is the EDS analysis depth, i.e. several micrometers. At the surrounding surface, where no bright deposits were formed, no Ce was detected (or the deposits were too thin to be detected by EDS) but only Si and O (Fig. S1, location 3). The presence of Ce in the deposits indicates that it was concentrated at particular sites at the surface, presumably at IMPs which are sites where cathodic reduction of oxygen proceeds and leads to release of hydroxyl ions and consequent increase in pH; a local pH increase to about 8.5 enables the precipitation of cerium oxide and /or hydroxide.[26,27,36]

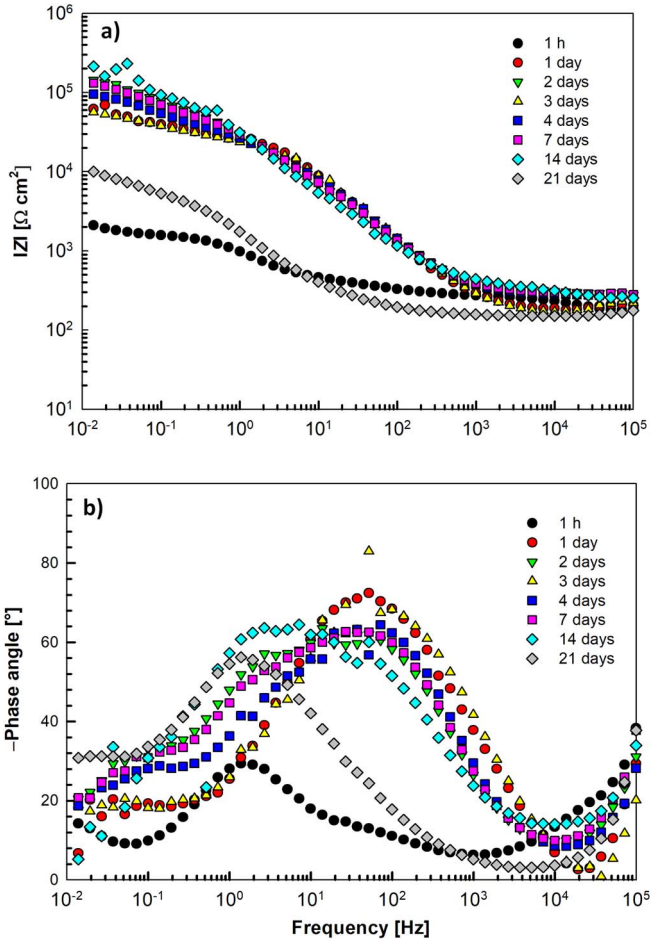

Figure 9. Bode plots of the magnitude of (a) impedance and (b) phase angle for a scribed GTS-Ce+GTS coating deposited on AA7075-T6 after various immersion times in 0.1 mol/L NaCl.

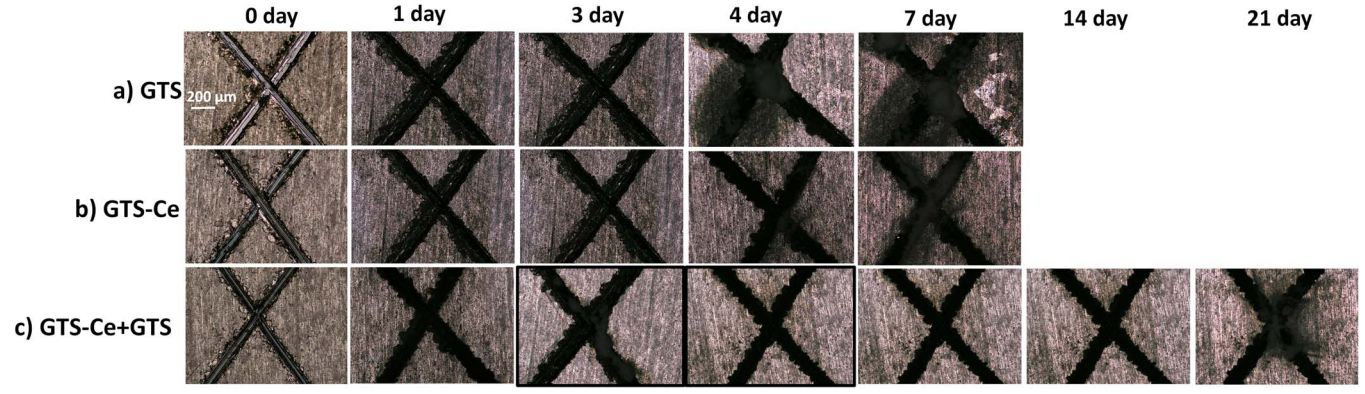

Figure 8. Optical microscope images of the cross shaped scribe on AA7075-T6 coated with (a) GTS, GTS-Ce and (c) GTS-Ce+GTS coatings after various immersion times in 0.1 mol/L NaCl. The depth of the scribe (~7 µm) was larger than the coating depth. The scale 200 µm (a, 0 day) is the same for all presented images.

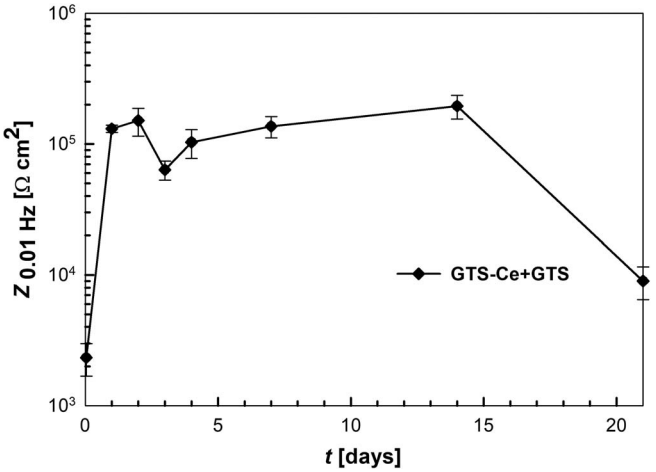

Figure 10. The impedance at 0.01 Hz, determined from Bode plots, of the magnitude of impedance vs. frequency recorded for a scribed GTS-Ce+GTS coating deposited on AA7075-T6 after various immersion times in 0.1 mol/L NaCl.

Corrosion behavior of scribed coatings in nacl solution.—The self-healing property of the coatings was addressed directly, using a cross-shaped scribe made at the surface. Scribe simulates the damage on/inside the coating, First, set of experiments was performed on GTS, GTS-Ce and GTS-Ce+GTS coatings scribed throughout the coating with a depth of 7.5 ± 0.4 μm, as determined by the profilometer. Self-healing ability was evaluated following immersion in 0.1 mol/L NaCl for up to 21 days. The propagation of the corrosion damage and self-healing process was monitored using optical microscope images of the scribe (Fig. 8). Secondly, EIS, SEM/EDS and XPS analyses were carried out at the scribed GTS-Ce+GTS coating (Figs. 9–17).

Immersion testing.—Corrosion on GTS and GTS-Ce at the scribe started after 4 days of immersion and spread over the surface (Figs. 8a, 8b). The width of the scribe on the GTS-Ce+GTS coating increased over 3 days of immersion and some corrosion products were observed (Fig. 8c). However, after 4 days of immersion the width of the scribe was diminished, indicating self-healing of the damage zone. Corrosion of the GTS-Ce+GTS coating was visible only after 21 days of immersion. Based on the obtained results, further study of the self-healing effect was concentrated on the GTS-Ce+GTS coating as GTS and GTS-Ce coatings did not show evidence of self-healing ability.

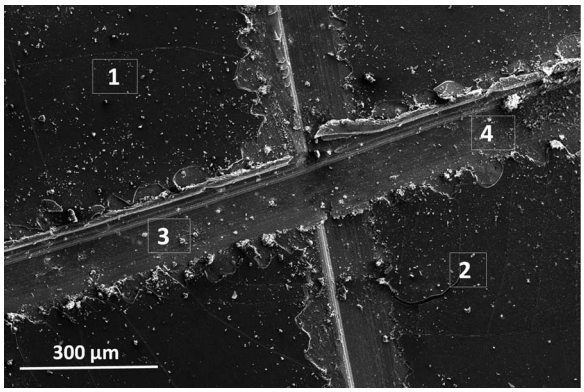

Figure 11. SEM/EDS analysis of the cross-shaped scribe on coating GTS-Ce+GTS, applied on AA7075-T6, after 4 days of immersion in 0.1 mol/L NaCl. The numbers 1–4 denote locations where EDS was carried out (Table II). The depth of the scribe (∼7 μm) was larger than the coating depth.

Electrochemical impedance analysis.—The corrosion properties of scribed GTS-Ce+GTS coatings were followed in situ during 21 days immersion in 0.1 mol/L NaCl using EIS. The dependence of the magnitude of impedance and phase angle on the frequency (Bode plots) after different immersion times is shown in Fig. 9. The corrosion resistance is represented by the values of the magnitude of the impedance determined at 0.01 Hz as a function of immersion time (Fig. 10). The shape of EIS spectra changed with increasing time of immersion. The most significant changes took place within 1 day of immersion, confirming improved corrosion resistance and an increase in $Z_{0.01\ Hz}$ value by more than one order of magnitude. With increasing immersion time up to 4 days the impedance plot changed to a more capacitive shape, with a pronounced linear range at the intermediate frequencies (Fig. 9a). At the same time the phase angle plot changed from that centered at intermediate frequencies to a plateau at the low frequencies (Fig. 9b). After 4 days immersion, a broad plateau extending up to 1 Hz is formed (Fig. 9a), reaching a phase angle of −70°

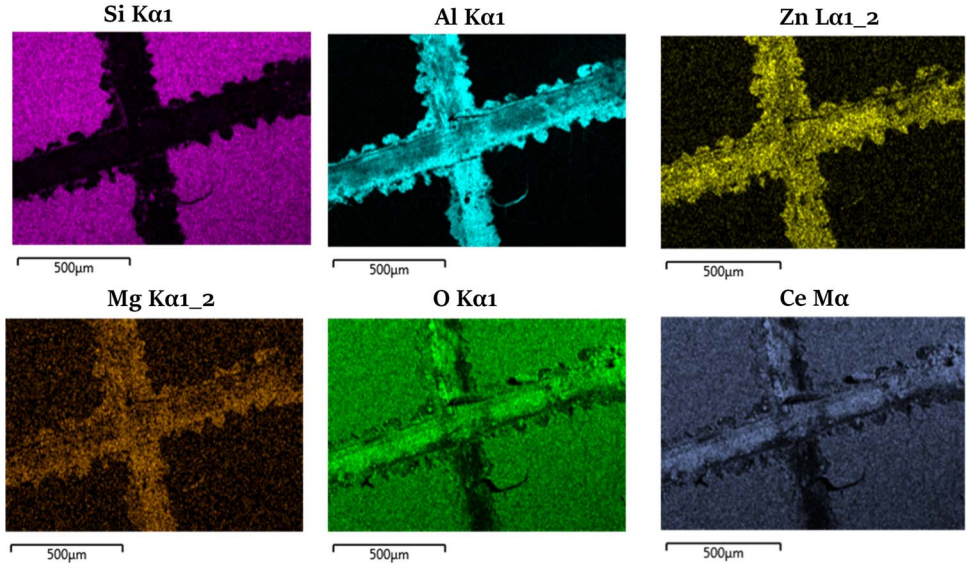

Figure 12. EDS mapping of cross-shaped scribed on GTS-Ce+GTS coating deposited on AA7075-T6 after 4 days of immersion in 0.1 mol/L NaCl (SEM image on Fig. 11). The depth of the scribe (∼7 μm) was larger than the coating depth.

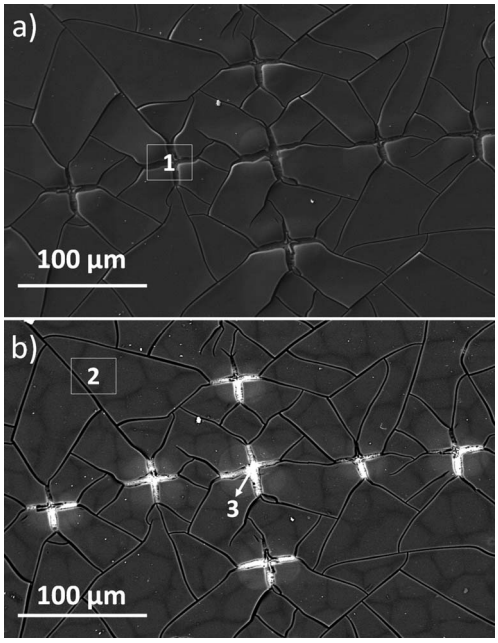

Figure 13. SEM images of cross-shaped Vicker's indents on a GTS-Ce+GTS coating deposited on AA7075-T6: (a) as-prepared, and (b) after being exposed to 0.1 mol/L NaCl for 4 days. The numbers 1–3 denote locations where EDS spectra were recorded (given in Supplement material as Fig. S2). The depth of the scribe (∼2–4 µm) was smaller than the coating depth but the indentations induced cracks.

(Fig. 9b). Spectra remained similar up to 14 days but, at longer immersion times, the beginning of dissolution is observed as a progressive reduction of $|Z|$ and ϕ at the low frequency side.

The value of $Z_{0.01\,Hz}$ of the scribed GTS-Ce+GTS coating increased gradually from $2{\cdot}10^3$ Ω cm^2 to 10^5 Ω cm^2 in the first 2 days (Fig. 10). After 3 days, a small drop in the value of $Z_{0.01\,Hz}$ was observed ($6{\cdot}10^4$ Ω cm^2), indicating that the corrosion process had commenced. After 4 days, however, the $Z_{0.01\,Hz}$ value regained its previous value (10^5 Ω cm^2) and then remained stable up to 14 days of immersion, confirming the healing of the scribed damage. After 21 days of immersion it again dropped to a smaller value ($9{\cdot}10^3$ Ω cm^2), indicating that the corrosion process proceeded gradually.

SEM/EDS and XPS analyses.—SEM analysis of the scribed zone after 4 days of immersion in 0.1 mol/L NaCl is presented in Fig. 11 accompanied by EDS analysis at locations 1–4 (Table II). Cerium was deposited on the surface at locations 1 and 2 and also within the scribe, at locations 3 and 4. Therefore, self-healing of the damage site observed during immersion is related to the deposition of cerium.

The presence of Ce was additionally corroborated using EDS mapping of the cross-shaped scribe (Fig. 12). Silicon and oxygen, the main components of the coatings, were detected only outside the scribe, since the coating was removed at the scribe. Aluminum and the alloying elements zinc and magnesium were identified within the scribe. Oxygen is also detected in the scribe associated with Al and Ce oxide/hydroxides formed during immersion. Finally, cerium was observed outside and inside the scribe, although in higher concentration in the latter site. This results evidences that the migration of Ce from the interior layer of the coating occurred and results in the deposition of Ce compound, not only on the surface, but also on the damaged area.

Second set of experiments was carried out on GTS-Ce+GTS sample scribe damaged within the coating, i.e. at indentations 2 to 4 µm deep, without reaching the underlying substrate. However, the indentation procedure itself damaged the coating and induced cracks (Fig. 13a) although the depth of indents did not reach the substrate, as evident by EDS spectrum (Fig. S2, spectrum 1) showing only Si. No such cracks were observed when using diamond blade (Fig. 11). The sample was then again immersed in 0.1 mol/L NaCl for 4 days and analyzed by SEM (Fig. 13b) and EDS at labelled positions (Fig. S2, spectra 2 and 3). Cerium was deposited mainly within the scribed

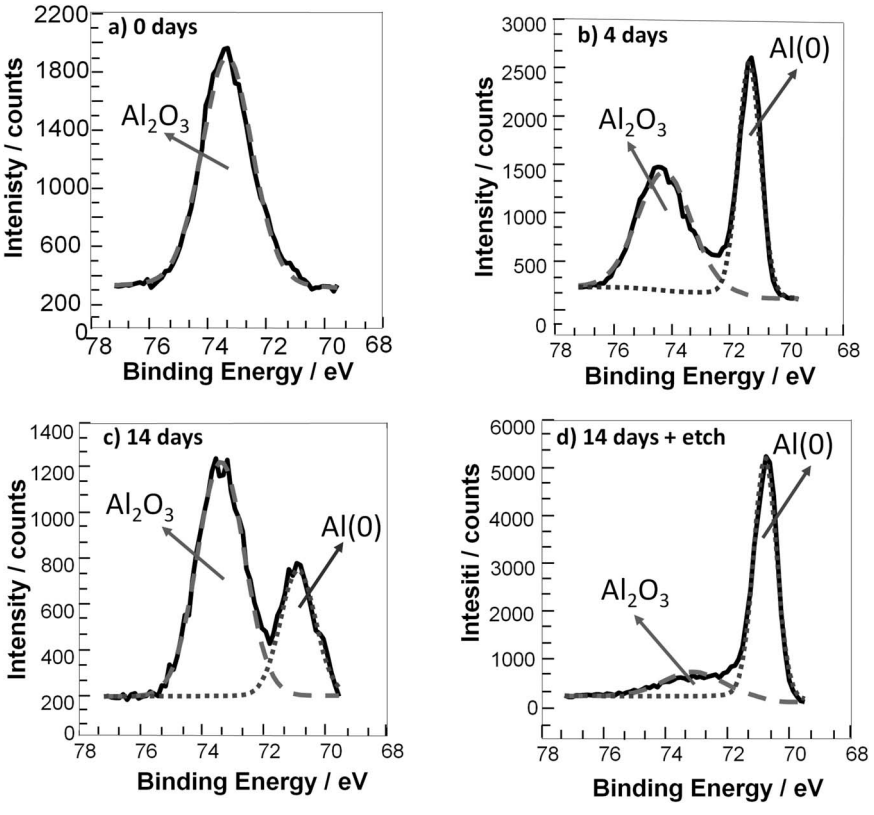

Figure 14. High resolution XPS Al 2p spectra recorded within a cross-shaped scribe on a GTS-Ce+GTS coating on AA7075-T6, before after 4 and 14 days immersion in 0.1 mol/L NaCl. After 14 days immersion the layer was etched using Ar^+ to reveal cerium deposits buried under aluminum oxide layer. Intensity of individual component peaks (expressed as%) is given in Table III. Solid curve denotes experimental data, and dashed and dotted curves are curve fitted component peaks.

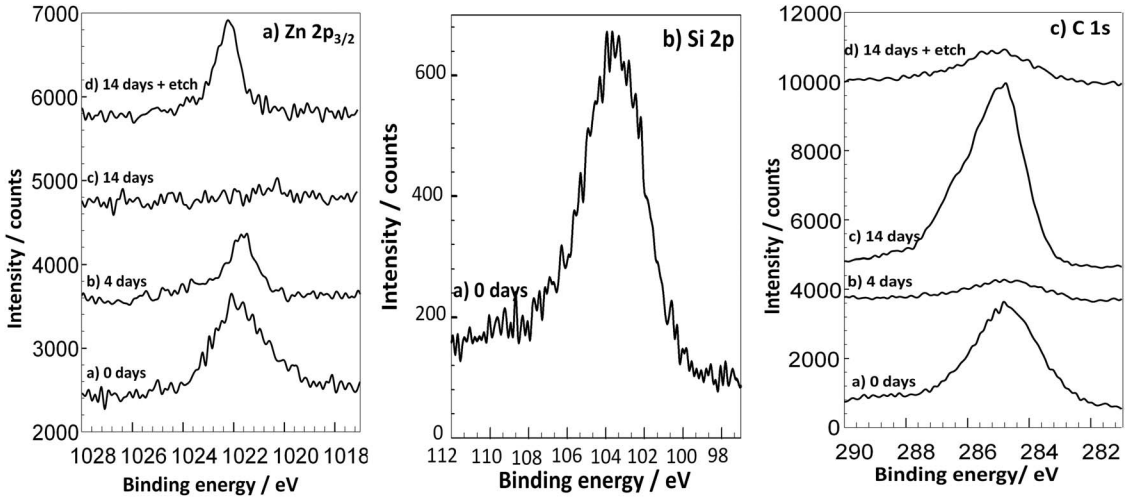

Figure 15. Non-normalized high resolution XPS (a) Zn $2p_{3/2}$, (b) Si 2p and (c) C 1 s spectra recorded within a cross-shaped scribe on a GTS-Ce+GTS coating on AA7075-T6, before and after 4 and 14 days immersion in 0.1 mol/L NaCl. After 14 days immersion the layer was etched using Ar^+ to reveal cerium deposits buried under aluminum oxide layer.

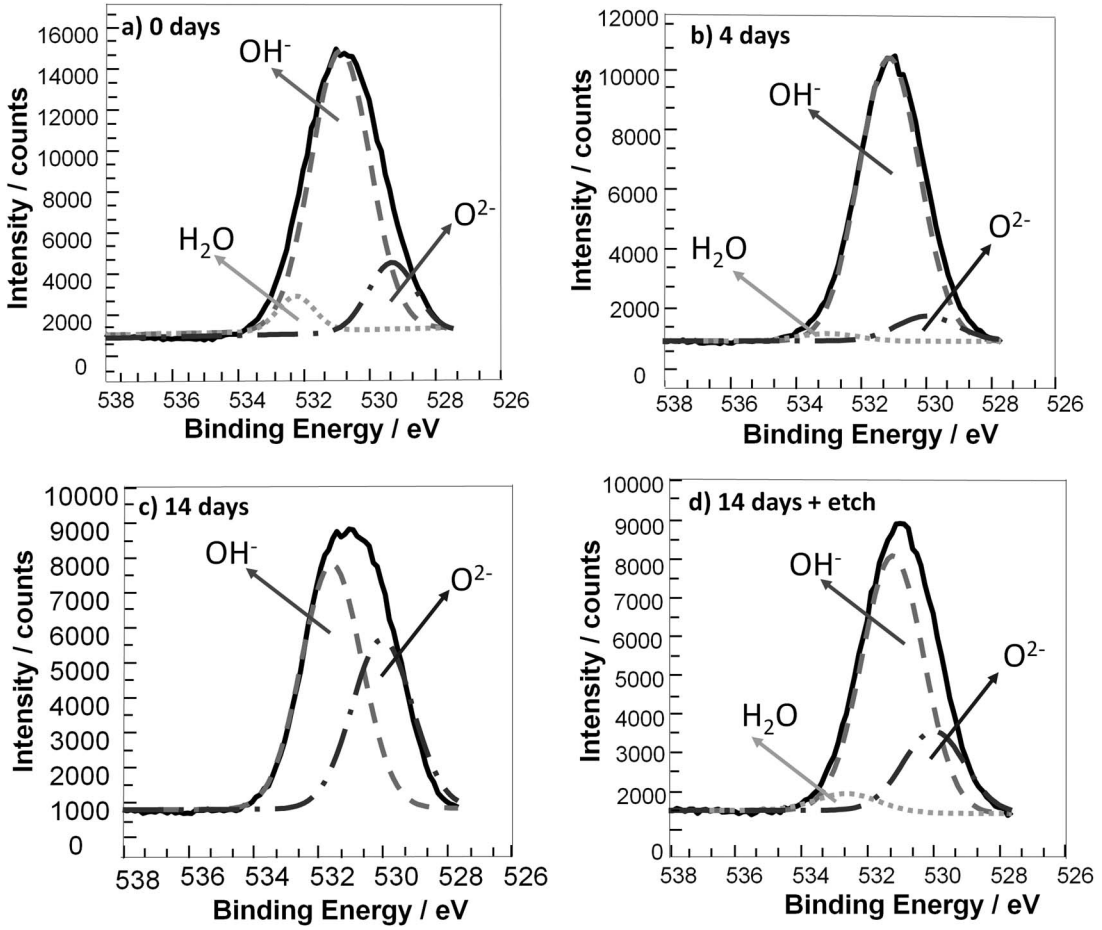

Figure 16. High resolution XPS O 1 s spectra recorded within a cross-shaped scribe on a GTS-Ce+GTS coating on AA7075-T6, before, and after 4 and 14 days immersion in 0.1 mol/L NaCl. After 14 days immersion the layer was etched using Ar^+ to reveal cerium deposits buried under aluminum oxide layer. Intensity of individual component peaks (expressed as %) is given in Table III. Solid curve denotes experimental data, and dashed and dotted curves are curve fitted component peaks.

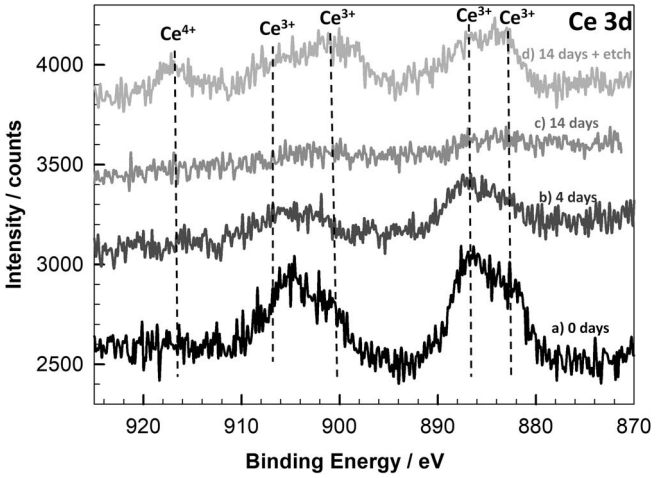

Figure 17. Non-normalized high resolution XPS Ce 3d spectra recorded within a cross-shaped scribe on a GTS-Ce+GTS coating on AA7075-T6, before, after 4 and 14 days of immersion in 0.1 mol/L NaCl. After 14 days immersion the layer was etched using Ar^+ to reveal cerium deposits buried under aluminum oxide layer.

area (label 3), while it was not detected out of the indents (label 2). Cerium had obviously migrated from the underlying coating and was deposited at damage sites after 4 days of immersion.

Therefore, in both cases – when scribed through the coating depth to reach the underlying substrate, or within the coating depth, the GTS-Ce+GTS coating was able to recover at damage site by the deposition of Ce-containing compound. However, the cracks induced by indentation propagate further during long-term immersion in NaCl (Fig. 13b) resulting in the observed cracking pattern. Therefore, indentation technique may be used as a complementary technique but that it may be more appropriate to use scribing procedure which does not induce damage (e.g. diamond blade).

In order to complement the EDS results and to study the oxidation state of Ce and elements of underlying substrate, XPS analysis was explored. The XPS spectra were recorded prior the immersion, and after 4 and 14 days of immersion in NaCl (Figs. 14–17). The diameter of XPS analysis is approximately 400 μm, i.e. similar to the diameter of the scribe. Therefore, the analysis identifies the elements coming from substrate (i.e. within the scribe) and the coating remnants (after being removed by diamond tip). The following elements were identified: Al and Zn originating from the substrate, O originating from the substrate and coating, and Si, C, and Ce related to the coating. Al 2p and O 1 s spectra were curve fitted, whilst Si 2p, Zn 2p, C 1 s and Ce 3d were described only qualitatively.

First, composition of surface prior immersion in NaCl will be discussed. Aluminum can originate from metal (71.0–71.5 eV) and aluminum oxide (74.6–74.8 eV) (Table III). A separate peak denoting the bonding between Al and Si, Al−O−Si, related to covalent silane-metal bonding[51] (73.2–73.6 eV) was not taken into account herein as we are concentrated on the processes within the scribe. Upon removal

Table II. Concentrations of elements obtained by EDS analysis at different locations on the cross shaped scribe on GTS-Ce+GTS coating deposited on AA7075-T6 after 4 days of immersion in 0.1 mol/L NaCl (locations 1–4) (SEM images in Fig. 11).

Location	Al [at.%]	O [at.%]	Si [at.%]	Zn [at.%]	Cu [at.%]	Ce [at.%]
1	70.9	23.8	7.9	1.9	/	0.1
2	60.3	34.8	3.0	4.2	1.7	0.1
3	70.4	21.7	1.7	5.2	1.0	0.3
4	62.4	25.6	2.8	6.7	2.2	0.2

Table III. Intensity of individual component peaks (expressed as %) obtained by curve fitting of XPS Al 2p (Al metal and Al_2O_3, Fig. 14) and O 1 s spectra (O^{2-}, OH^- and H_2O peaks, Fig. 16) recorded within scribe in GTS-Ce+GTS coating on AA7075-T6 before and after 4 and 14 days immersion in 0.1 mol/L NaCl. After 14 days, surface was etched to remove the oxide layer.

Immersion time	Al [%]	Al_2O_3 [%]	O^{2-} [%]	OH^- [%]	H_2O [%]
0	0	100.0	14.8	80.0	6.2
4 days	45.2	54.8	7.7	90.2	2.1
14 days	28.5	71.5	37.7	62.3	0
14 days and etching	78.4	21.6	21.0	75.2	3.8

of sol-gel coating within the scribe, Al oxide forms spontaneously. Therefore, prior immersion, only Al oxide is identified within the scribe (Fig. 14a, Table III). A small amount of zinc is also detected originating from the AA7075-T6 substrate (Fig. 15a). The center of the Zn $2p_{3/2}$ peak is located at 1022.5 eV. XPS Zn 2p spectrum cannot allow an exact differentiation between Zn metal and ZnO due to small chemical shift of only 0.9 eV.[60] Instead, Zn LMM spectra should be used for this purpose but due to a small amount of Zn such analysis would be ambiguous. Silicon originates from the coating. The Si 2p peak is centered at 103.7 eV (Fig. 15b). This peak could be comprised of several component peaks: Si−OH, Si−O−Si and Si−O−Al.[51] Carbon C1s peak is centered at 284.8 eV and relates to adventitious carbon and aliphatic carbon (C−C) present in the coating (Fig. 15c). However, the peak is quite broad which may be related to the presence of (C−O) bonds at 286.5 eV in the coating structure, as proposed also based on FTIR spectra.[43] More detailed analysis of Si 2p and C 1 s peaks is beyond the scope of this study and requires NMR analysis.

The O 1 s spectra can be separated into three component peaks: oxide, O^{2-}, at approx. 530 eV, hydroxide, OH^-, at approx. 531 eV, and water, H_2O, at approx. 533 eV (Fig. 16a).[50,61] Deconvolution of the peak shows that the native layer is composed mostly of hydroxide (Table III).

Prior immersion, four main peaks were observed in the Ce 3d spectrum, at 882.6, 886.6, 901.8 and 905.1 eV (Fig. 17). The XPS 3d spectra of cerium compounds show a complex satellite structures derived mainly from ligand to metal charge transfer transitions, i.e. O 2p → 4f transitions.[62] The Ce spectrum of Ce(III) compound is composed of four peaks corresponding to two spin-orbit features at 880.9, 885.5, 899.1 and 903.4 eV.[62] The spectrum of Ce(IV) compound is composed of six peaks corresponding to three spin-orbit features at 882.7, 886.6, 898.3, 901.3, 907.3 and 916.7 eV. It appears that prior immersion cerium is present primarily in the Ce(III) oxidation state, although some peaks may indicate the presence of small amount Ce(IV) state (i.e. at E_b higher than 905 eV). It should be noted that the concentration of Ce in sols GTS-Ce+GTS coating is very low (0.05 mol/L). Consequently, the concentration in the coating is also low, as evidenced by weak signal which is poorly defined. After 4 days of immersion the metal Al peak appears in the spectra (Fig. 14b), indicating that in the course of immersion Al oxide may be dissolved exposing Al metal. The intensities of Zn and C peaks decreased, and the Si peak disappeared, probably due to the coverage by deposited Ce-based layer. (Fig. 15). The O 1 s spectrum is still mainly composed of hydroxide contribution (Fig. 16b, Table III). The presence of tetravalent cerium may be indicated by the peak at 916.7 eV which distinguishes Ce(III) and Ce(IV) compounds (Fig. 17).[62] Taking into account that two types of oxide/hydroxide are formed (Al- and Ce-based), oxygen peak could be curve fitted by additional OH^- and/or O^{2-} component, as proposed previously.[50,63] Further study using well prepared standards would be required to corroborate further differentiation between two components.

After 14 days of immersion, however, cerium was not identified within the scribe (Fig. 17). This may be the consequence of progressive formation of an aluminum oxide film within the scribe in the course of prolonged immersion in 0.1 mol/L NaCl (Fig. 14c, Table III). At

the same time, Zn signal disappeared, and that of C 1 significantly increased which may be related to precipitation of coating remnants within the scribe (Fig. 15c). As the analysis diameter is similar to scribe diameter it is difficult to differentiate the origin of the signal (i.e. from scribe or surrounding coating remnants). It seems certain, however, that formation of Al oxide covered the underlying cerium oxide deposits. This was proved using Ar^+ etching which removed approximately 26 nm of Al oxide layer (Fig. 17). After etching, cerium was again detected within the scribe showing the characteristic peak of Ce(IV) at 916.7 eV thus proving that Ce(III) is oxidized to Ce(IV) species. The Al_2O_3 peak disappeared and that of Al and Zn metals increased (Figs. 14d, 15a).

Proposed mechanism of cerium inhibition and self-healing in GTS-Ce+GTS coatings.—The proposed self-healing mechanism and the role of Ce ions in the self-healing effect in the GTS-Ce+GTS coating can be summarized as follows. During immersion in aerated NaCl, Ce^{3+} ions from the underlying GTS-Ce coating can oxidize to Ce^{4+} through different pathways, assisted by O_2 or H_2O_2.[16,28] SEM/EDS and XPS analyses have confirmed that deposition of cerium within the cross-shaped scribe increased after 4 days' immersion. The oxidation state of cerium changes from mainly Ce(III) to Ce(IV). This process takes place at the substrate/electrolyte interface, i.e. within the coating. As the self-healing experiments were carried out at the scribe exposed to electrolyte, during the course of immersion the formation of aluminum oxide takes place as well which then covers the cerium oxide deposits underneath.

The self-healing ability may be achieved by the migration of $Ce(OH)_2^{2+}$ to local damaged regions where these ions precipitate as $Ce(OH)_4$ and CeO_2, which are highly insoluble.[16,28,36] According to thermodynamic calculations by Yasakau et al., $Ce(OH)_2^{2+}$ are stable only at pH below 3, thus their presence at neutral and slightly alkaline pH may be questionable.[36] However, results obtained in the present study show that the migration of Ce ions takes place as the healing of corrosion damage site is noticed. The exact speciation of migrating species could not be confirmed despite using different analytical techniques (XPS, EDS). In the literature the exact nature of migrating species has not been yet proven; this issue remains to be investigated further. The self-healing cycle can be repeated as long as Ce^{3+} are present in the coating.[33] It was proposed that the Ce^{3+}/Ce^{4+} redox reaction is dynamic, and proceeds readily in both directions.[59] According to results obtained using SEM/EDS, XPS and EIS, the self-healing effect of the GTS-Ce+GTS coating is operative, even after 14 days of immersion in NaCl solution, because of the presence of Ce^{3+} ions in the coating. Under these conditions the repetitive cycle of (i) Ce^{3+} to Ce^{4+} oxidation, (ii) $Ce(OH)_2^{2+}$ migration to damaged site, and (iii) transformation $Ce(OH)_2^{2+}$ to $Ce(OH)_4$ can continue.[50] The final step in the mechanism is the formation of insoluble CeO_2 at cathodic sites, providing additional hindering of the corrosion process.[35]

At a longer immersion time (21 days), the magnitude of impedance decreased, indicating diminished self-healing ability. However, the overall coating stability was still much higher than that of the coating without cerium (GTS), or in the case of GTS-Ce (Fig. 5).

Conclusions

1. Three types of sol-gel coatings prepared based on TEOS, GPTMS, SiO_2 and $Ce(NO_3)_3$ and applied on AA7075-T6 substrates. This was done in order to produce a coating which would exhibit a self-healing ability in chloride environment. Although all three coatings (GTS, GTS-Ce and GTS-Ce+GTS) improved the corrosion resistance of the substrate during 80 days immersion in NaCl, only the GTS-Ce+GTS coating containing cerium in the inner layer showed the self-healing properties. The GTS coating provides only barrier protection. GTS-Ce coating may be destabilized either due to the modified structure of the coatings due to incorporation of Ce, or due to progressive outward leaching of cerium which limits its role in the self-heling activity. Locking of Ce in the inner layer inhibits the destabilization of the coating and prolong its activity in the self-healing process.
2. Active role of cerium in the inhibition process was proved by long-term EIS measurements and immersion test on unscribed and scribed coatings. Self-healing of the GTS-Ce+GTS coating starts after 4 days of immersion in 0.1 mol/L NaCl. After an initial decrease, the impedance at low frequency increased by more than one order of magnitude proving the self-healing process. It is thus demonstrated that the migration of cerium ions occurred. Cerium is deposited on the alloy surface and within the cross-shaped scribe, in the form of hydroxide. The latter insoluble compound reduces the kinetics of the cathodic reaction and contributes to self-healing of the coating.
3. Although gradually transformed into Ce(IV) hydroxide, both oxidation states (Ce(III) and Ce(IV)) were identified, even after 14 days of immersion, indicating that the self-healing process was still operative.
4. All systems in the present work were found to have promising applications and could be regarded as potential replacements for hazardous chromate conversion coatings.
5. Future study will focus on the compatibility of these coatings with organic top coatings, e.g. adhesion and the corrosion performance of such full systems.

Acknowledgments

The authors acknowledge the financial support from the Slovenian Research Agency (research core funding No. P2-0393 and the project "Lightweight alloys based on aluminum as materials with increasing potential in the transportation industry", ID J1-6734). U. Tiringer acknowledges an Ad Futura scholarship for financing her stay at the CSIC. The authors thank dr. A. Drnovšek for SEM/EDS analysis, dr. J. Kovač for valuable discussion of XPS data, T. Filipič, MSc, for spectra acquisition, dr. P. Panjan for help in making Vicker´s indents at coated samples and Prof. R.H. Pain for proof reading the manuscript.

ORCID

Ingrid Milošev https://orcid.org/0000-0002-7633-9954

References

1. C. Vargel, *Corrosion of aluminum*, 1st. ed., Elsevier, Amsterdam, The Netherlands, (2004).
2. J. R. Davis, *Corrosion of aluminum and aluminum alloys*, ASM International, United States of America, (1999).
3. G. Kufman, *Introduction to aluminum alloys and tempers*, 1st. ed., ASM International, United States of America, (2000).
4. *CMCA(UK)* (2017) https://www.cmcauk.co.uk/reach-authorisation-list-update-imminent-sunset-dates/.
5. M. W. Kendig and R. G. Buchheit, *CORROSION*, **59**, 379 (2003).
6. J. W. Bibber, *Met. Finish.*, **99**, 15 (2001).
7. T. P. Chou, C. Chandrasekaran, and G. Z. Cao, *J. Sol-Gel Sci. Technol.*, **26**, 321 (2003).
8. R. B. Figueira, C. J. R. Silva, and E. V. Pereira, *J. Coat. Technol. Res.*, **12**, 1 (2014).
9. I. Milošev, B. Kapun, P. Rodič, and J. Iskra, *J. Sol-Gel Sci. Technol.*, **74**, 447 (2015).
10. R. L. Twite and G. P. Bierwagen, *Prog. Org. Coat.*, **33**, 91 (1998).
11. S. Zheng and J. Li, *J. Sol-Gel Sci. Technol.*, **54**, 174 (2010).
12. J. Wen and G. L. Wilkes, *Chem. Mater.*, **8**, 1667 (1996).
13. N. Pirhady Tavandashti, S. Sanjabi, and T. Shahrabi, *Mater. Corros.*, **62**, 411 (2011).
14. G. Schottner, *Chem. Mater.*, **13**, 3422 (2001).
15. M. L. Zheludkevich, I. M. Salvado, and M. G. S. Ferreira, *J. Mater. Chem.*, **15**, 5099 (2005).
16. I. Santana, A. Pepe, E. Jimenez-Pique, S. Pellice, I. Milošev, and S. Ceré, *Surf. Coat. Technol.*, **265**, 106 (2015).
17. A. J. Vreugdenhil, V. N. Balbyshev, and M. S. Donley, *J. Coat. Technol.*, **73**, 35.
18. R. N. Peres, E. S. F. Cardoso, M. F. Montemor, H. G. de Melo, A. V. Benedetti, and P. H. Suegama, *Surf. Coat. Technol.*, **303**, Part B, 372 (2016).
19. A. Durán, Y. Castro, M. Aparicio, A. Conde, and J. J. de Damborenea, *Int. Mater. Rev.*, **52**, 175 (2007).
20. N. N Voevodin, N. T Grebasch, W. S Soto, L. S Kasten, J. T Grant, F. E Arnold, and M. S Donley, *Prog. Org. Coat.*, **41**, 287 (2001).
21. N. C. Rosero-Navarro, S. A. Pellice, Y. Castro, M. Aparicio, and A. Durán, *Surf. Coat. Technol.*, **203**, 1897 (2009).

22. J. Ballarre, I. Manjubala, W. H. Schreiner, J. C. Orellano, P. Fratzl, and S. Ceré, *Acta Biomater.*, **6**, 1601 (2010).
23. N. N. Voevodin, J. W. Kurdziel, and R. Mantz, *Surf. Coat. Technol.*, **201**, 1080 (2006).
24. B. R. W. Hinton, *J. Alloys Compd.*, **180**, 15 (1992).
25. B. R. W. Hinton, D. R. Arnott, and N. E. Ryan, *Metals Forum*, **7**, 211 (1984).
26. L. Li, A. L. Desouza, and G. M. Swain, *The Analyst*, **138**, 4398 (2013).
27. A. J. Davenport, H. S. Isaacs, and M. W. Kendig, *Corros. Sci.*, **32**, 653 (1991).
28. A. J. Aldykiewicz, A. J. Davenport, and H. S. Isaacs, *J. Electrochem. Soc.*, **143**, 147 (1996).
29. W. Trabelsi, P. Cecilio, M. G. S. Ferreira, and M. F. Montemor, *Prog. Org. Coat.*, **54**, 276 (2005).
30. G. Yoganandan, K. Pradeep Premkumar, and J. N. Balaraju, *Surf. Coat. Technol.*, **270**, 249 (2015).
31. M. L. Zheludkevich, R. Serra, M. F. Montemor, K. A. Yasakau, I. M. Miranda Salvado, and M. G. S. Ferreira, *Electrochimica Acta*, **51**, 208 (2005).
32. N. C. Rosero-Navarro, L. Paussa, F. Andreatta, Y. Castro, A. Durán, M. Aparicio, and L. Fedrizzi, *Prog. Org. Coat.*, **69**, 167 (2010).
33. N. C. Rosero-Navarro, M. Curioni, Y. Castro, M. Aparicio, G. E. Thompson, and A. Durán, *Surf. Coat. Technol.*, **206**, 257 (2011).
34. X. Zhong, Q. Li, J. Hu, F. Luo, and Y. Dai, *Prog. Org. Coat.*, **69**, 52 (2010).
35. M. L. Zheludkevich, K. A. Yasakau, A. C. Bastos, O. V. Karavai, and M. G. S. Ferreira, *Electrochem. Commun.*, **9**, 2622 (2007).
36. K. A. Yasakau, M. L. Zheludkevich, S. V. Lamaka, and M. G. S. Ferreira, *J. Phys. Chem. B*, **110**, 5515 (2006).
37. K. Aramaki, *Corros. Sci.*, **44**, 1375 (2002).
38. M. Forsyth and B. Hinton, *Rare Earth-Based Corrosion Inhibitors*, p. 347, Elsevier, (2014).
39. L. Paussa, N. C. Rosero Navarro, D. Bravin, F. Andreatta, A. Lanzutti, M. Aparicio, A. Durán, and L. Fedrizzi, *Prog. Org. Coat.*, **74**, 311 (2012).
40. N. C. Rosero-Navarro, S. A. Pellice, A. Durán, S. Ceré, and M. Aparicio, *J. Sol-Gel Sci. Technol.*, **52**, 31 (2009).
41. N. C. Rosero-Navarro, S. A. Pellice, A. Durán, and M. Aparicio, *Corros. Sci.*, **50**, 1283 (2008).
42. H. Wang and R. Akid, *Corros. Sci.*, **50**, 1142 (2008).
43. U. Tiringer, A. Durán, Y. Castro, and I. Milošev, *J. Sol-Gel Coat. Technol.*, **85**, 546 (2018).
44. L. Paussa, N. C. Rosero-Navarro, F. Andreatta, Y. Castro, A. Duran, M. Aparicio, and L. Fedrizzi, *Surf. Interface Anal.*, **42**, 299 (2010).
45. N. C. Rosero-Navarro, S. A. Pellice, A. Durán, and M. Aparicio, *Corros. Sci.*, **50**, 1283 (2008).
46. J-B. Cambon, J. Esteban, F. Ansart, J-P. Bonino, V. Turq, S. H. Santagneli, C. V. Santilli, and S. H. Pulcinelli, *Mater. Res. Bull.*, **47**, 3170 (2012).
47. F. Mansfeld and Y. Wang, *Mater. Sci. Eng. A*, **198**, 51 (1995).
48. P. Chakraborty Banerjee and R. K. Singh Raman, *Electrochimica Acta*, **56**, 3790 (2011).
49. A. Zomorodian, F. Brusciotti, A. Fernandes, M. J. Carmezim, T. Moura e Silva, J. C. S. Fernandes, and M. F. Montemor, *Surf. Coat. Technol.*, **206**, 4368 (2012).
50. R. V. Lakshmi, S. T. Aruna, C. Anandan, P. Bera, and S. Sampath, *Surf. Coat. Technol.*, **309**, 363 (2017).
51. I. Milošev, Ž. Jovanović, J. B. Bajat, R. Jančić-Heinemann, and V. B. Mišković-Stanković, *J. Electrochem. Soc.*, **159**, C303 (2012).
52. S. Adhikari, K. A. Unocic, Y. Zhai, G. S. Frankel, J. Zimmerman, and W. Fristad, *Electrochimica Acta*, **56**, 1912 (2011).
53. J. A. Syed, S. Tang, and X. Meng, *Appl. Surf. Sci.*, **383**, 177 (2016).
54. S. P. Knight, M. Salagaras, A. M. Wythe, F. De Carlo, A. J. Davenport, and A. R. Trueman, *Corros. Sci.*, **52**, 3855 (2010).
55. P. Rodič and I. Milošev, *J. Electrochem. Soc.*, **163**, C85 (2016).
56. N. Birbilis and R. G. Buchheit, *J. Electrochem. Soc.*, **155**, C117 (2008).
57. R. G. Buchheit, *J. Electrochem. Soc.*, **142**, 3994 (1995).
58. O. Gharbi, N. Birbilis, and K. Ogle, *J. Electrochem. Soc.*, **163**, C240 (2016).
59. R. G. Buchheit, M. A. Martinez, and L. P. Montes, *J. Electrochem. Soc.*, **147**, 119 (2000).
60. I. Milošev and H.-H. Strehblow, *J. Electrochem. Soc.*, **150**, B517 (2003).
61. J. Beran, S. Hishita, K. Mašek, V. Matolín, and H. Haneda, *Ceram. Int.*, **40**, 323 (2014).
62. E. Bêche, P. Charvin, D. Perarnau, S. Abanades, and G. Flamant, *Surf. Interface Anal.*, **40**, 264 (2008).
63. E. Paparazzo, *Superlattices Microstruct.*, **105**, 216 (2017).